



The Impact of Surface Temperature Heterogeneity on Near-Surface Heat Transport

Travis Morrison¹ · Marc Calaf¹ · Chad W. Higgins² · Stephen A. Drake³ · Alexei Perelet¹ · Eric Paradyjak¹

Received: 8 April 2020 / Accepted: 10 April 2021 / Published online: 11 May 2021
© The Author(s), under exclusive licence to Springer Nature B.V. 2021

Abstract

Experimental closure of the surface energy balance during convective periods is a long-standing problem. With experimental data from the Idealized horizontal Planar Array experiment for Quantifying Surface heterogeneity, the terms of the temperature-tendency equation are computed, with an emphasis on the total derivative. The experiment occurred at the Surface Layer Turbulence and Environmental Science Test facility at the U.S. Army Dugway Proving Ground during the summer of 2019. The experimental layout contained an array of 21 flux stations over a 1 km² grid. Sensible heat fluxes show high spatial variability, with maximum variability occurring during convective periods. Maximum variability in the vertical heat flux is 50–80 W m⁻² (median variability of 40%), while in the horizontal flux, it is 200–500 W m⁻² (median variability of 48% for the streamwise and 40% for the spanwise fluxes). Ensemble averages computed during convective afternoon periods show large magnitudes of horizontal advection (48 W m⁻³ or 172 K h⁻¹) and vertical flux divergence (13 W m⁻³ or 47 K h⁻¹). Probability density functions of the total derivative from convective cases show mean volumetric heating rates of 43 W m⁻³ (154 K h⁻¹) compared to 13 W m⁻³ (47 K h⁻¹) on non-convective days. A conceptual model based on persistent mean flow structures from local-surface-temperature heterogeneities may explain the observed advection. The model describes the difference between locally-driven advection and advection driven by larger-scale forcings. Of the cases examined, 83% with streamwise and 81% with spanwise advection during unstable periods are classified as locally driven by nearby surface thermal heterogeneities.

Keywords Advection · Convective boundary layer · IPAQS campaign · Surface energy balance · Temperature tendency

✉ Travis Morrison
travis.morrison@utah.edu
Eric Paradyjak
eric.parddyjak@utah.edu

¹ Department of Mechanical Engineering, University of Utah, Salt Lake City, Utah, USA

² College of Agricultural Sciences, Oregon State University, Corvallis, Oregon, USA

³ Department of Physics, University of Nevada, Reno, Nevada, USA

1 Introduction

Understanding the mechanisms that affect the surface energy balance (SEB) between the land surface and the atmosphere is essential to enhancing our ability to forecast the earth–atmosphere system (Williams et al. 2009; Blyth et al. 2010). It is only through a solid understanding and quantification of the energy exchange at the land–atmosphere interface that one can develop simplifications and parametrizations to be used in forecasting models (e.g., numerical weather prediction (NWP) models, and climate models). For the most part, there is consensus on the major roles of net radiation, turbulent fluxes, and ground heat flux on the SEB. However, when the SEB is stripped of its assumptions, terms such as advection arise, which are rarely studied experimentally (Oncley et al. 2007; Cuxart et al. 2015, 2016; Garcia-Santos et al. 2019). Here, we present terms in the temperature-tendency equation computed with experimental data, motivated by the limited understanding of advection and turbulent flux divergence on the SEB over heterogeneous surfaces.

The one-dimensional SEB (Eq. 1) can be derived from the temperature-tendency equation assuming steady-state conditions, horizontal homogeneity, and the absence of subsidence. Net radiation (term I) drives the SEB, which in the simplified one-dimensional budget is balanced by the sum of the turbulent sensible heat flux (term II), the latent heat flux (term III), and the ground heat flux, which includes the energy storage (term IV)

$$\underbrace{R_n}_I = \underbrace{H}_II + \underbrace{H_L}_III + \underbrace{G}_IV. \quad (1)$$

Despite the apparent simplicity of the integral SEB equation, a remaining residual (i.e., imbalance) of approximately 25% is common, specifically during convective periods (Foken 2008). There is an extensive literature detailing the various limitations associated with attempting to experimentally quantify the SEB. For example, Katul et al. (1999) used experimental data and Kanda et al. (2004) used numerical studies to examine the representativeness of a single flux tower compared to spatially distributed towers when computing terms of the SEB. Meanwhile, Finnigan et al. (2003) suggested that short averaging periods could be a reason for the lack of low-frequency information in the turbulent flux, which is often underestimated over vegetated and hilly surfaces (Panin et al. 1998; Wilson et al. 2002). Grachev et al. (2019) have shown that increasing averaging periods to seasonal scales minimizes the SEB closure without consideration of the ground or storage terms in cases with wet and dry soils. Gao et al. (2017) used modal decomposition to correct and improve the SEB closure over a wet field. Alternatively, Heusinkveld et al. (2004) found that over a desert playa the ground heat flux and storage terms are a large portion of the SEB and found near closure during nocturnal periods. Meanwhile, Higgins (2012) found through an a posteriori analysis of SEB data collected at the Surface Layer Turbulence and Environmental Science Test (SLTEST) facility, Dugway, Utah, that large residuals in the SEB were due to spatial variability in the energy storage, rather than flux underestimation.

Terms that arise from ignoring the aforementioned assumptions in the SEB have also been examined in the literature. Experiments have studied the role of temperature advection (Oncley et al. 2007; Cuxart et al. 2015, 2016; Garcia-Santos et al. 2019), vertical flux divergence (Nakamura and Mahrt 2006; Zhang et al. 2010; Gao et al. 2016, 2017; Mahrt et al. 2018), and storage (Meyers and Hollinger 2004; Oliphant et al. 2004; Xu et al. 2019), to name a few. Nakamura and Mahrt (2006) found an imbalance between the temperature tendency and the vertical turbulent flux divergence for nocturnal boundary layers. The radiative flux divergences were unable to explain the residual, stressing the importance of horizontal

advection even in weakly thermal heterogeneous terrain. Oncley et al. (2007) studied horizontal advection during the EBEX experiment and reported a contribution of 30 W m^{-2} (5–10% of the residual). Meanwhile, Cuxart et al. (2016) found, based on an order of magnitude analysis, that advection could be of the same order of magnitude as the traditionally accepted residual for the SEB. Moreover, Gao et al. (2017) reported the possibility that the existence of a phase shift between vertical velocity component fluctuations (w') and water vapour density fluctuations (q') could be responsible for the non-closure of the SEB, further hypothesizing that advection could be the agent responsible for the phase shift between the fluctuating variables as induced by large, slow-moving eddies (i.e., secondary circulations) (Foken et al. 2011). However, as reported in Foken et al. (2011), and illustrated in Kanda et al. (2004) and Steinfeld et al. (2008), to achieve a successful measurement of these elusive but relevant secondary circulations, time-synchronized, spatially distributed measurements are necessary.

The plant-canopy community has extensively studied the transport of CO_2 , heat, and water from the perspective of the differential transport equations. Extensive research has been performed on the advection transport of heat and water for the study of evapotranspiration (Prueger et al. 1996; Figuerola and Berliner 2005; Alfieri et al. 2012; Higgins et al. 2013). Of particular relevance is the work of Moderow et al. (2007), who found that horizontal advection in the temperature-tendency equation was significant for a forest, while horizontal flux divergence was not at night-time. Moreover, a variety of experiments have solely focused on CO_2 transport (Feigenwinter et al. 2004; Aubinet et al. 2003, 2005, 2010). Of relevance, Feigenwinter et al. (2004) established an experimental site at one of the CarboEurope-FLUX sites in Tharandt, Germany, to measure the advective transport of CO_2 . Meanwhile the ADVEX CarboEurope-Integrated Project advection campaign specifically used three of the CarboEurope-FLUX sites to study the underestimation of the CO_2 flux in forested canopies during nocturnal periods (Aubinet et al. 2010).

We hypothesize that by removing these assumptions and studying the temperature-tendency equation directly (over an idealized surface), we can gain a better understanding of the SEB and its closure. The temperature-tendency equation can be written in a Lagrangian form as the balance between *Sources* and *Sinks* of heat and the time rate-of-change of temperature of the flow (Eq. 2a). Explicitly, the total derivative can be expanded and the *Sources* and *Sinks* written in Eulerian form as (Eq. 2b)

$$\frac{D\bar{T}}{Dt} = \text{Sources} + \text{Sinks}, \tag{2a}$$

$$\frac{DT}{Dt} = \underbrace{\frac{\partial \bar{T}}{\partial t}}_I + \underbrace{\bar{u}_i \frac{\partial \bar{T}}{\partial x_i}}_II + \underbrace{\frac{\partial \bar{u}'_i \bar{T}'}{\partial x_i}}_III = \underbrace{\alpha \frac{\partial^2 \bar{T}}{\partial x_i^2}}_IV - \underbrace{\frac{1}{\rho c_p} \frac{\partial \bar{R}_{ni}}{\partial x_i}}_V - \underbrace{\frac{L_v}{c_p} \frac{\partial \bar{u}'_i q'}{\partial x_i}}_VI. \tag{2b}$$

Here, the tendency equation (Eq. 2b) is presented in differential form using index notation (Stull 1988), where T is temperature, t is time, u_i is the i^{th} component of the velocity vector, x_i is the spatial coordinate, R_{ni} is the net body source of radiation, q is the specific humidity, and ρ , c_p , L_v , and α are the density, isobaric heat capacity, latent heat of vaporization, and the thermal diffusivity of air, respectively. Correspondingly, the overbar denotes an ensemble or time average and the prime indicates a fluctuation from the mean. Specifically, term I represents the mean storage of heat, term II is the mean advection of heat by the bulk flow, term III is the mean divergence of the turbulent sensible heat flux, term IV is the mean molecular diffusion of heat, term V is the mean radiative flux divergence, and term VI is the

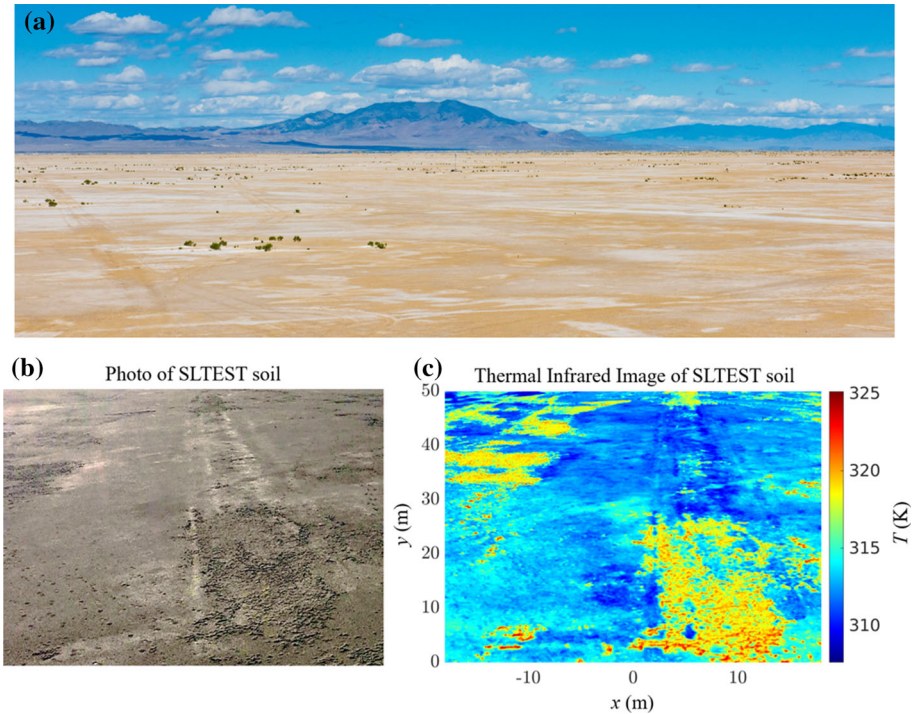


Fig. 1 **a** Photograph of the SLTEST facility, illustrating the site's uniform surface roughness and long uninterrupted fetch. Large differences in surface albedo from the spatially varying salt crust can be observed. **b** A close-up photograph from the thermal image site, and **c** an image of radiative surface temperature of the desert playa taken during the 2019 IPAQS (1047 LT (local time = UTC - 6 h) on 9 July 2019). Both **b** and **c** are presented without camera distortion to show all surface details, such that the axes are approximate distances. Both **b** and **c** were captured from the 10-m LA1 flux tower looking north-west onto the experimental site (see Figs. 2 and 3 for a representation of the field site). Note the scale of the patchiness as well as the range of temperatures measured (17 °C difference)

latent-heat-flux divergence. Through the following analysis, we provide quantification and analysis of the total derivative (i.e., left-hand side of Eq. 2b).

To accurately assess terms in Eq. 2b, we use data from the Idealized Planar Array experiment for Quantifying Spatial heterogeneity (IPAQS) campaign, which were obtained in a dry-lake-bed desert environment at the SLTEST facility in western Utah, U.S.A. The IPAQS dataset was acquired with a unique horizontal grid of turbulence measurements at a resolution of ~ 200 m, over a highly idealized and quasi-canonical surface with an extent of about 1 km^2 . The SLTEST facility was chosen for its idealized characteristics (Fig. 1), which include a homogeneous rough surface (with a low aerodynamic roughness length $z_0 < 1$ mm), and a long uninterrupted fetch (Malek 2003). Despite these ideal characteristics, the SLTEST facility has large underlying surface thermal and moisture heterogeneities (Hang et al. 2016; Morrison et al. 2017). Figure 1b is a photograph of the SLTEST facility during the 2019 IPAQS campaign and Fig. 1c is a thermal image of the same surface taken at the same time. For illustration purposes, Fig. 1c shows uncorrected (i.e., surface emissivity taken as unity) surface radiative temperature heterogeneities, with a range of 17 K, and with characteristic length scales of approximately 30–50 m. These large thermal heterogeneities arise due to the soil's variable surface radiative and thermal properties. For example, in Fig. 1a, variable

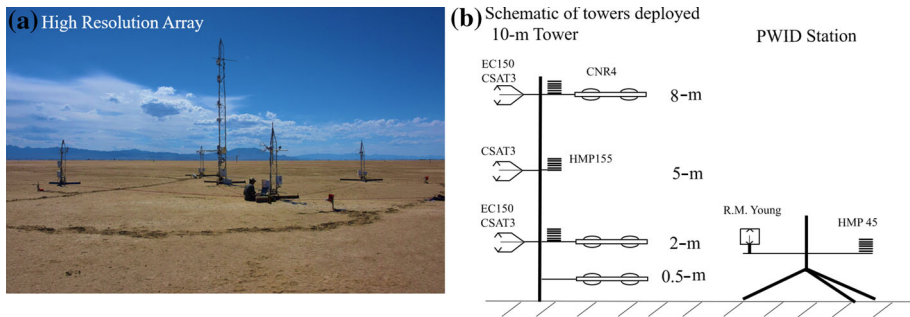


Fig. 2 Deployment details of the 2019 IPAQS campaign. **a** Image of the high-resolution array taken from the south-west. Note the stencil of 2-m towers surrounding the 10-m tower. **b** A schematic of the 10-m tower deployed at the high-resolution array. The EC150 refers to the Campbell Scientific EC150 measuring fast response CO₂ and moisture, the CSAT3 denotes the Campbell Scientific CSAT3 sonic anemometer, the R.M. Young refers to the R. M. Young sonic anemometer, the HMP refers to the Vaisala slow response temperature and relative humidity sensor, and the thin black line inside the sonic anemometers represents a fine-wire thermocouple. Note that only the central high-resolution array tower included the CNR4s to capture the net radiation at multiple heights [seen in (a)], and the EC150s. The PWID Station schematic denotes a typical PWID (black circles in Fig. 3) which were deployed in a horizontal grid with 200-m spacing

patches of opaque salt crust (white surfaces) at the surface have a higher albedo and are generally cooler than the adjacent dark areas, which are absent of salt crust and thus have a lower albedo, thus, providing an ideal site with uniform surface roughness and surface temperature heterogeneity for evaluating the closure of the temperature-tendency budget.

Specifically, our study quantifies and analyzes the advection terms (Eq. 2b, term II), and its corresponding turbulent flux divergence (term III) with experimental data. In addition, variability associated with thermal stratification and secondary circulations is investigated. This variability is hypothesized to relate to the non-closure of the SEB. Below, in Sect. 2, the details of the dataset used and the corresponding post-processing analysis are presented, and in Sect. 3, general meteorological conditions of the period of interest. A detailed analysis of the component variables of the advection and turbulent flux divergence terms is presented in Sect. 4, leading to the computed terms of the total derivative presented in Sect. 5. Finally, a discussion of the results is presented in Sect. 6 in the context of the SEB closure problem with the concluding remarks presented in Sects. 6 and 7.

2 Methods

The following section presents the data-acquisition and data-treatment methodologies used to compute the terms of the temperature-tendency equation. Section 2.1 presents a detailed explanation of the IPAQS field campaign. Section 2.2 describes how the data were post-processed and treated to compute the terms in Eq. 2b.

2.1 Experimental Dataset

The IPAQS campaign was carried out at the U.S. Army Dugway Proving Ground, at the SLTEST facility, 137 km south-west of Salt Lake City, Utah (40°8'5.9" N, 113°27'7.8" W). The site is characterized by a wide basin stretching ~ 65 km east–west, with a long, flat,

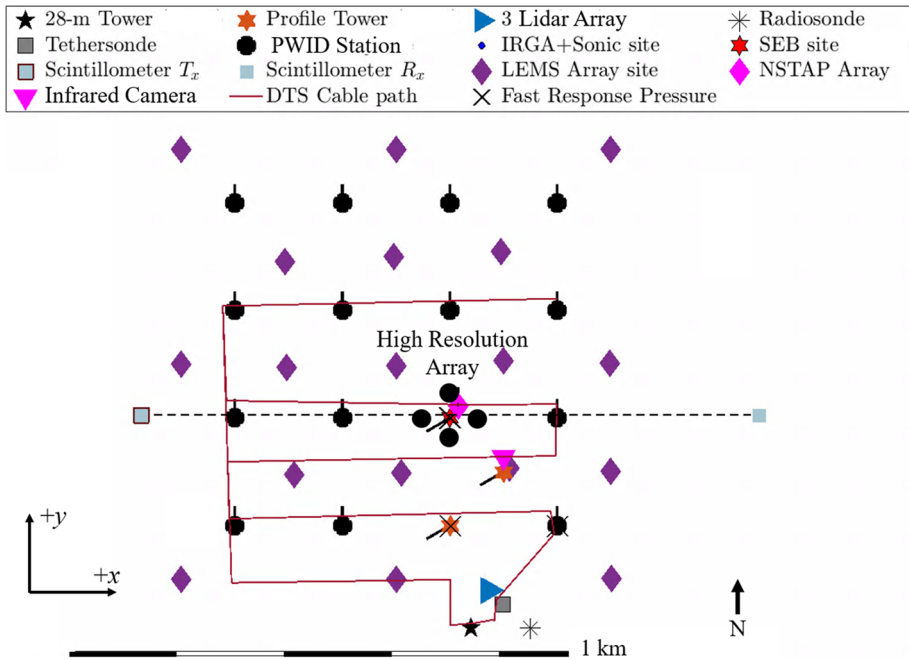


Fig. 3 Deployment details of the 2019 IPAQS campaign. The legend denotes symbols used for each instrument, where the nanoscale temperature array probes are referred to as the NSTAP Array. The High Resolution Array label denotes the high-resolution array is located slightly south-east of the centre of the main array. The array is orientated with the cardinal directions, which facilitates the use of a standard meteorological coordinate system for computing horizontal derivatives. Furthermore, details of the instruments deployed over the array are provided in Table 1

north–south fetch (~ 130 km), with topographical variations of less than 1 m km^{-1} (Metzger 2002; Malek 2003; Hang et al. 2016; Jensen et al. 2016). The site is a desert playa, with air temperatures often above 40°C at local solar noon and falling below 20°C at night. Given the arid climate, the relative humidity is extremely low, rarely above 20%. At larger topographical scales, a slight declination from south to north in the basin often results in nightly southerly, and daily north-westerly, wind directions in the summer (Jeglum 2016).

Figure 3 is a schematic of the experimental layout for IPAQS19 and a summary of the instruments deployed is given in Table 1. The IPAQS campaign was designed to capture scales resolved in large-eddy simulations (LES) (scales from $\sim 1 \text{ km}$ – 10 m) while stretching over a grid cell of a typical NWP model ($\sim 1 \text{ km}$). Portable weather instrumentation data systems (PWIDS) (Fig. 3c) equipped with 8100 R. M. Young ultrasonic anemometers (Traverse City, Michigan) and fine-wire thermocouples (measuring the three components of velocity and temperature at 20 Hz, respectively) were placed on a coarse grid covering an area of $800 \times 800 \text{ m}^2$ with 200-m spacing orientated to true north (black circles). In Fig. 3, the orientation of the sonics is denoted by the tick from the black circles. Open source Arduino-based low-cost energy-budget measurement stations (LEMS, Gunawardena et al. 2018) were deployed on an array offset 100 m from the main PWID array and measured the 2-m horizontal velocity components (two-dimensional sonic anemometer), air pressure, air temperature, and relative humidity. In addition, they measured incoming solar radiation, radiative surface temperature, and soil temperatures at depths of 0.05 and 0.20 m (purple diamonds).

Table 1 Detailed instrument information for the IPAQS instrumentation

Instrument	Variables measured	Sampling frequency (Hz)	Tower locations
CSAT3	u, v, w, T	20	High resolution array, 28-m tower, 10-m towers
EC150	$\text{CO}_2, \text{H}_2\text{O}$	20	High resolution array, 10-m tower at 2 m and 8 m, high resolution array east tower, high resolution array south tower
R. M. Young	u, v, w, T	20	PWID stations
Finewire thermocouple	T	20	PWID stations, high resolution array, 28-m tower, 10-m towers
HMP155	T, RH	1	10-m tower, high resolution array
HMP45	T, RH	1	PWID stations, 28-m tower
LEMS	$u, v, R_n, T_a, T_s, P, RH$	0.1	LEMS stations

Three 10-m towers were placed in the array, represented with red stars in Fig. 3, and schematically represented in Fig. 2b. Each 10-m tower was equipped with three sonic anemometers (CSAT3, Campbell Scientific, Logan, Utah) at 2 m, 5 m, and 8 m oriented perpendicular to the anticipated mean wind direction (240°) (Jeglum 2016). To capture smaller-scale motions, an additional high-resolution array composed of four 2-m towers, with 10-m spacing was deployed near the centre of the larger array Fig. 2a. One of the three 10-m towers was placed at the centre of the high-resolution array. In addition to the aforementioned instruments, this 10-m tower was equipped with infrared gas analyzers (IRGA EC150, Campbell Scientific, Logan, Utah) coupled with sonic anemometers (CSAT3A, Campbell Scientific, Logan, Utah) at 2 m and 8 m for fast-response moisture and CO_2 measurements and their respective gradients. This tower also comprised three radiometers (CNR4, Kipp & Zonen, The Netherlands) at 0.5 m, 2 m, and 8 m to measure the four components of the net radiation and to serve as our SEB station. The neighbouring 2-m tall high-resolution towers were equipped with CSAT3 sonic anemometers, with EC150 analyzers at the east and south towers. Moreover, the west station included an array of soil temperatures at depths 0.01, 0.025, 0.05, 0.10, 0.15, 0.25, 0.70 m, and two self-calibrating ground heat flux plates (HFP01, Hukseflux, the Netherlands) at a depth of 0.05 m and spaced 1.5 m apart. It is also important to note that the high-resolution array is used to compute the advection terms (see Fig. 2 for details). At the southern end of the coarse array, a 28-m tower was equipped with CSAT3 anemometers at heights of 20 m and 25 m. All instruments were surveyed (Leica Total Station, Norcross, Georgia) which provides accurate spacing within ± 0.5 m. Data loggers were time synchronized with a global positioning system (GPS16-HVS, Garmin, Olathe, Kansas). The resulting sub 1-ms temporal synchronization provides the accuracy needed to compute spatial and temporal derivatives during data analysis.

In addition, a distributed temperature sensing system (ULTIMA DTS, Silixa, United Kingdom), measured the approximate surface temperature with a 1.5-mm diameter white fibre optic every 0.125 m and 1 s throughout the array and up and down the 28-m mast, for a total length of ~ 5 km (Fig. 3 purple line). To measure surface thermal heterogeneities at high spatial and temporal resolution, a thermal imager (VarioCAM HD[®]800, InfraTec, Plano, Texas) with an uncooled microbolometer detector (spectral range of 7.5 to 14 μm) and a resolution

of 1024×768 measured the surface temperature over the entire array and the high-resolution array during daytime periods at 10 Hz. For an understanding of boundary-layer dynamics aloft, daily tethersoundings and twice-daily radiosoundings were made at the southern end of the array most weekdays. This overview indicates the instrumentation used here. The IPAQS field deployment also included measurements from wind lidars (Jungo et al. 2018), scintillometry, and nanoscale hot-wire anemometry (Huang et al. 2018).

2.2 Data Treatment

Data were acquired from 17 June 2019 to 15 July 2019. The period was characterized by a wide range in air temperature, variable relative humidity, and wind speeds. The most complete dataset was captured from 1 July 2019 to 15 July 2019 and provides the opportunity to assess the vertical and horizontal terms of the temperature-tendency equation (Eq. 2b). The data were processed with Utah Turbulence in Environmental Studies Process and Analysis Code (UTESPac) (Jensen et al. 2016), which first applies conditional despiking (Vickers and Mahrt 1997) and computes means on 5-min windows. The 5-min averages were then used to compute a global planar fit (Wilczak et al. 2001) over the two-week period of interest. Despite the local meteorology suggesting a binary wind direction (e.g., primarily northerly or southerly wind direction), the global planar fit was chosen to capture the persistent differences in the flow over the two-week period. The data were then rotated into a meteorological coordinate system, such that southern wind directions correspond to a positive v -component and western wind directions correspond to a positive u -component. A multiresolution decomposition indicated that all turbulent scales of motion are accounted for in 1000-s sampling during unstable and stable atmospheric stability periods (Vickers and Mahrt 2003). Therefore, perturbations and temporal means were computed using 30-min windows after linear detrending. Further sensitivity analysis shows that over the entire campaign, the median percent difference between vertical fluxes computed from a constant detrend and linear detrend at the central high-resolution array tower was -4% (a positive percent difference indicates the linear detrended term was larger than the constant detrended term). Meanwhile, during transition periods where stationarity is not always achieved this value decreases to -22% during the hours before/during sunrise (0400 LT–0700 LT) and -37% for the hours during/after sunset.

Lastly, as advection calculations are very sensitive to the mean fine-wire temperature, a temperature collocation was performed. The error associated with measuring temperature (found to be $\approx 1.7^\circ\text{C}$) was corrected by fitting a second-order polynomial to a reference temperature (taken as the 2-m fine-wire thermocouple at the centre of the high-resolution array). Note that this measured error in air temperature is a result of inherent limitations associated with current technology. Details outlining this methodology can be found in Appendix 1. The horizontal derivatives were calculated using a central finite difference [$\mathcal{O}(\delta^2)$ accuracy] around the centre of the high-resolution (HiResC) array using the surrounding PWID stations. Explicitly, stations HiResN and HiResS for $\partial/\partial y$, HiResE and HiResW for $\partial/\partial x$ at scale δ (10 m). Finally, the vertical derivative terms were computed by fitting the 2-m, 5-m, and 8-m signals with a second-order Lagrange polynomial at the central high-resolution array tower.

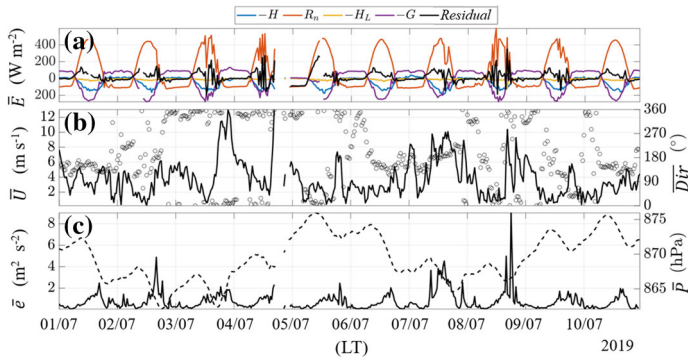


Fig. 4 Time series (30-min averages) of the general meteorological conditions (**b, c**) and components of the SEB according to Eq. 1 **a** during IPAQS19 from 1 July to 11 July 2019. The orange line presents the net radiation, the blue line presents the sensible heat flux, the purple line is the ground heat flux, the yellow line is the latent heat flux, and the black line is the residual. Note that the sensible, latent, and ground heat fluxes have all been plotted such that when all terms are added together, the sum equals the residual (i.e. $= R_n - H - H_L - G$). Panel **b** shows the wind speed (solid black line) and wind direction (black circles), and **c** shows the turbulence kinetic energy (solid black line) and air pressure (black dashed line)

3 Background Meteorological Conditions

Data collected during IPAQS19 from 1 July 2019 to 11 July 2019 are presented here. Raw variables such as wind speed, wind direction, and air temperature, provide background meteorological conditions for understanding the characteristics of the site during data acquisition and the evaluation of Eq. 2b. For a full review of the site's climatology, we recommend Jeglum (2016).

Figure 4 presents the general conditions observed at the IPAQS19 field site over the 11 days of data collection at the 2-m height at the central high-resolution-array tower (SEB station). From top to bottom, Fig. 4a presents the SEB following Eq. 1, Fig. 4b illustrates the wind speed (\bar{U}) and wind direction (Dir), and Fig. 4c shows the turbulence kinetic energy (TKE, \bar{e}), and atmospheric pressure (P).

The dates of 1, 5, 6, and 10 July were found to be ideal clear-sky convective days, while 3, 4, and 8 July were characteristically stormy. Despite this variability, the mean SEB residual remained approximately 25%. Moreover, the data show that, due to the site's arid climate, the latent heat flux is never above 20 W m^{-2} during its peak in the late afternoon. The ground heat flux, mostly on the clear-sky days, has a strong diurnal pattern and is the largest component next to the net radiation, which is consistent with previous measurements at the site (Higgins 2012; Hang et al. 2016). The residual, while small at night, remains in the range $50\text{--}120 \text{ W m}^{-2}$ of the budget during convective periods.

Figure 4b presents the 2-m wind speed and wind direction for the same period. A wide range in wind speeds was observed over the testing period. In particular, between 1 July and 3 July, the wind speeds were between weak and moderate (1 m s^{-1} and 6 m s^{-1}), with flow from the north, switching to flow from the south by 3 July. Between 3 July and 9 July, periodic storm fronts provided periods with high wind speeds, up to 12 m s^{-1} , except for 6 July, which was characterized by clear skies and moderate wind speeds. From 10 July to 11 July, we observed another clear-sky day accompanied by moderate northerlies.

The wind direction over these days was more binary than the wind speed, either uniformly southern or northern, except on 2 July and 9 July. With north–south running mountain ranges

to the east and west of the SLTEST facility, the local flows are expected to follow these results. However, from climatological reports, we anticipated steady flow from the north during the daytime period, followed by a switch during the evening transition to flow from the south, induced by the playa breeze. Figure 4c shows the air pressure, indicating that two low-pressure events (2 July to 5 July and 6 July to 10 July) occurred during the presented period that may have influenced the anticipated wind directions which are observed over longer datasets.

Lastly, Fig. 4c presents 30-min averages of TKE. Over the 11 days examined, a diurnal pattern of $\bar{\epsilon}$ is observed, which peaks during the afternoon convective period at approximately $2 \text{ m}^2 \text{ s}^{-2}$ and decays rapidly during the evening transition. It is interesting to note that the most significant peaks in $\bar{\epsilon}$ occurred during the two afternoons corresponding to low-pressure periods (2 July to 5 July and 7 July to 9 July). Analysis from large-scale weather models indicates that the large values in $\bar{\epsilon}$ on 2 July and 7 July arise from local convective thunderstorms, while the peak on the afternoon of 9 July is from a frontal passage.

4 Spatial Variability of Terms in the Temperature Tendency Equation

To build an understanding of the spatial scope of the IPAQS database and the range of variables observed to compute the terms of the total derivative (Eq. 2b), raw velocities, temperatures, and turbulence quantities across the entire array are presented. It should be noted that this section provides data from the entire $800 \times 800 \text{ m}^2$ array, but the following advection analysis in Sect. 5 only uses data from the high-resolution array. We present spatial snapshots from the data over one averaging period, as well as time series to better understand the spatial and temporal variability above the a priori quasi-canonical SLTEST site. Furthermore, this analysis provides a unique view of spatially distributed in situ observations over what is considered an idealized grid cell in a NWP model.

4.1 Advection: Mean Velocity and Temperature Fields

The terms used in the calculation of the advection term in Eq. 2b (Term II) require the mean velocity and temperatures throughout time and space. This information is presented in Figs. 5 and 6 correspondingly to build a stronger understanding of the input variables, which are used later in Sect. 5. Spatial statistics provide a proxy for the potential advection over the experimental site. Thus, when a wide range of temperatures and wind speeds are observed, advection may provide a strong source of heat transport.

Figure 5 presents the temporal statistics observed over two days of data collection, illustrating that the standard deviation remains small over time compared with the values for the spatial range (difference between the spatial maximum and minimum value measured at a given time within the array). Explicitly, during the daytime periods, the range observed in the v -component in Fig. 5a peaks to 1.8 m s^{-1} on 9 July. However, the standard deviation remains $< 0.5 \text{ m s}^{-1}$ over this same period, which indicates that the standard deviation is not capturing the range of values observed over the entire array, and hence may not be providing insight into the potential advection for the site. Statistically, this is important because the standard deviation illustrates that the potential for advection over the entire grid may be weak. However, the range shows that there are local regions within the grid where advective transport may be important. Figure 5c presents the same statistics for 2-m air temperature, illustrating that the observed surface temperature variability shown in Fig. 1 ($\Delta T = 17 \text{ K}$)

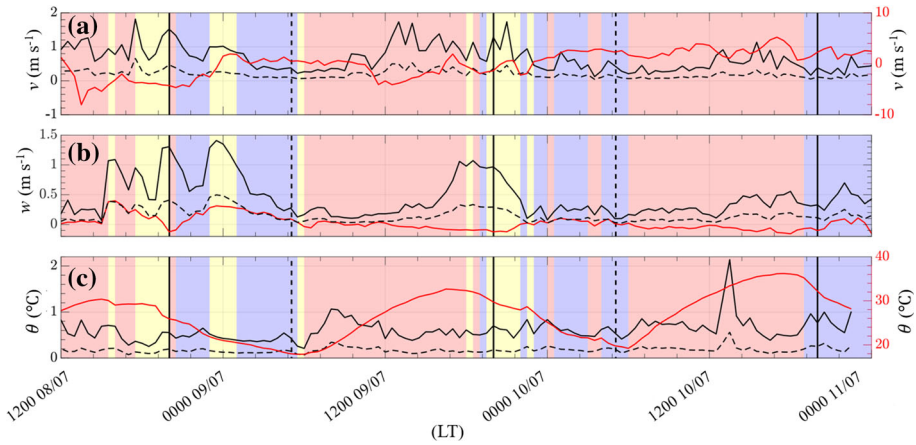


Fig. 5 Time series from 8 July to 11 July of the 2-m 30-min averaged **a** v - and **b** w -velocity components and **c** air temperature. Lines represent the space averaged (red line), spatial standard deviation (black dashed line), and spatial range (solid black line) at the coarse-grid stations (200-m spacing). The vertical black solid and dashed lines represent sunset and sunrise, respectively. The background shading denotes the local stability (z/L) with blue, yellow, and red representing stable ($z/L \geq 0.1$), neutral ($0.1 \geq z/L \geq -0.1$), respectively, and unstable periods ($z/L \leq -0.1$). The right-hand axes represent values for the spatial mean in (a) and (c)

has significantly decreased to $< 2 \text{ }^\circ\text{C}$ at 2 m. Moreover, during extended periods of neutral stability (yellow shading), the most significant spatial variability of the wind speeds is observed, specifically during the evening transition of 8 July and 9 July. On 10 July, which was characterized by moderate wind speeds and high pressure, the spatial range remained under 1 m s^{-1} for the v -component and under 0.5 m s^{-1} for the w -component. These observations suggest that when a period of low pressure is occurring, the potential for strong wind speeds (advection) is high.

Figure 6 presents a colour map of the mean v -component (\bar{v}), vertical velocity component \bar{w} , and air temperature at 2 m (\bar{T}). Figure 6a, b illustrates the local mean differences in velocity components observed over the array. These mean perturbations show the potential for shear and buoyancy differences across a 1-km^2 grid and are large given the idealized test site where the measurements were collected. Specifically, in the north-east quadrant of Fig. 6a, b, we observe the v -component ranging from 1.0 m s^{-1} to 1.8 m s^{-1} and w -velocity component from -0.2 m s^{-1} to 0.1 m s^{-1} . This shows that, over a $200 \times 200 \text{ m}^2$ subsection of the site, persistent mean differences are present nearby, bringing into question the assumption of horizontal homogeneity over this and seemingly more complex sites. To understand the impact of these persistent local differences on advection, we look to the temperature. In Fig. 6c, we observe a fairly uniform temperature across the grid. However, the data also illustrate the potential for advection. For example, over this period, in the high-resolution array, horizontal temperature differences over 10 m are $\approx 0.1 \text{ }^\circ\text{C}$. If we assume a wind speed during the period of 1 m s^{-1} , we would observe an advection of the order of 10 W m^{-3} .

4.2 Turbulent Flux Divergence: Turbulent Flux Fields

The spatial and temporal variability of the turbulent sensible heat flux, which arises in Term III in Eq. 2b, is shown in Figs. 7 and 8. Figure 7 presents the temporal variability of the

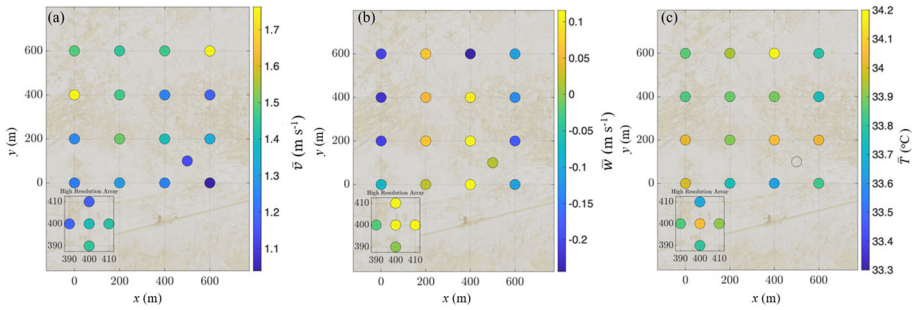


Fig. 6 Colour contours of the 30-min temporally-averaged **a** v -component, **b** w -component, **c** and air temperature observed at each station at 2 m on 10 July at 1400 LT. The background of each figure is the satellite image of the SLTEST facility where each instrument was deployed (USGS 2018). The colour of each station is denoted by the colourbar

turbulent fluxes, while Fig. 8 provides the spatial variability of the heat flux for a 30-min average in time.

In Fig. 7, each space-averaged turbulence quantity follows a diurnal trend peaking during convective periods, with the exceptions of the horizontal terms, which are at a maximum during the near-neutral periods. Figure 7a, b shows that the spatial averages are significantly smaller than the range of values observed over the array. It is unclear why such a large range of turbulence values occur. However, it suggests that single-point measurements are lacking important spatial information about turbulent transport. These results and their impact on flux divergence are discussed further in Sect. 5.

Figure 7c presents the vertical component of the turbulent sensible heat flux, illustrating a strong diurnal pattern with spatial averages peaking near solar noon at 120 W m^{-2} and a spatial variability (standard deviation) of approximately half the magnitude of the flux (60 W m^{-2}). This suggests that during unstable periods, an individual tower observation of sensible heat flux is likely to vary by $\pm 50\%$ compared with the average across the array. Figure 7 also shows that turbulence can vary substantially during the night. For example, on the night of 8–9 July, turbulent fluxes are nearly zero, while on the night of 9–10 July, significantly higher turbulent values are observed.

Figure 8 shows colour contours of sensible heat flux from each 2-m tower for the same 30-min period shown in Fig. 6 (10 July 2019 at 1400 LT). In Fig. 8a we observe values of $\rho c_p \overline{u'T'}$ ranging from -120 W m^{-2} to 100 W m^{-2} over the $1 \times 1 \text{ km}^2$ grid. Moreover, we observe negative values populating the south-west corner of the array. Meanwhile, the north-east corner of the array contains positive values. In Fig. 8b, we observe values of $\rho c_p \overline{v'T'}$ ranging from -210 W m^{-2} to 85 W m^{-2} over the $1 \times 1 \text{ km}^2$ grid, illustrating the typical spatial distribution of horizontal turbulence quantities that lead to the statistics shown in Fig. 7. These figures demonstrate how a wide range of measured horizontal fluxes can lead to a small spatial average, but a large spatial standard deviation, indicating local measurements may be large and not representative of the mean. Additionally, it is observed that the spatial variability of these horizontal fluxes are larger on highly convective days. It is hypothesized that this occurs due to persistent mean structures which occupy the array during periods with free-convective characteristics. The range of measured vertical sensible heat fluxes (Fig. 8c) extends from 75 W m^{-2} to 148 W m^{-2} . Moreover, over distances of merely 10 m in the high-resolution array (inset Fig. 8), measured values of $\rho c_p \overline{w'T'}$ range from 105 W m^{-2} to 155 W m^{-2} , illustrating the strong variability in the heat flux in neighbouring areas. While the

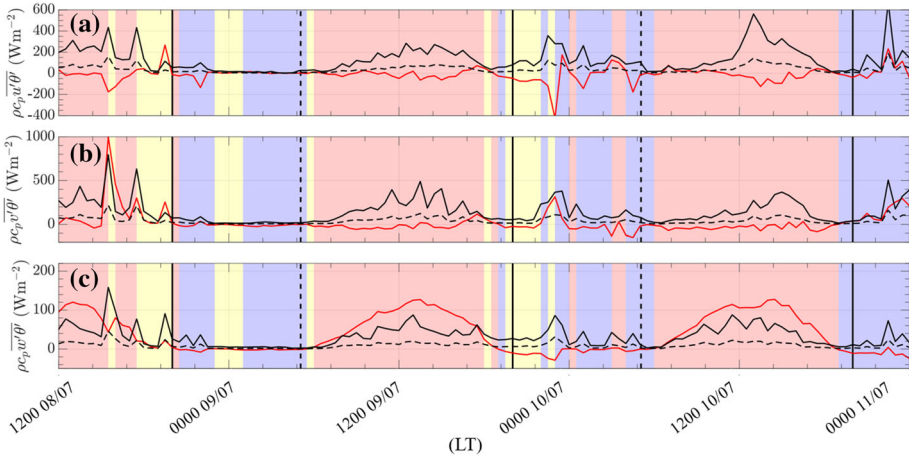


Fig. 7 Time series from the 8 July to 11 July of the 2-m, 30-min turbulent heat fluxes for the **a** x-component, **b** y-component, and **c** vertical component. Lines represent the space averaged (red line), spatial standard deviation (black dashed line), and spatial range (solid black line) from the coarse grid towers (200-m spacing). The vertical black solid and dashed lines represent sunset and sunrise, respectively. The background shading denotes the local stability (z/L) with blue, yellow, and red representing stable, neutral, and unstable periods

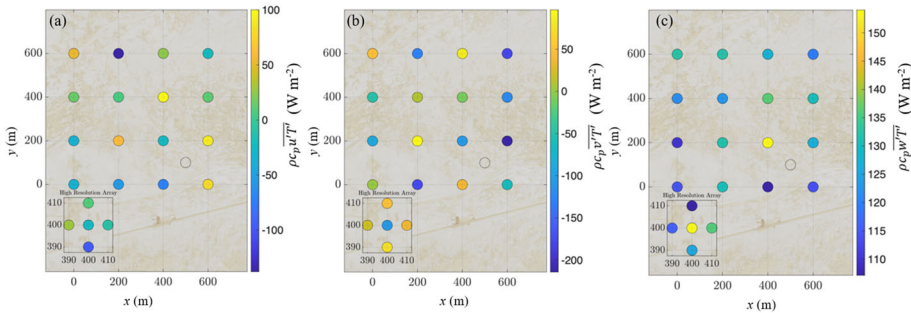


Fig. 8 Colour contours of the turbulent sensible heat flux for the **a** x-component, **b** y-component, and **c** z-component computed at each station at 2 m for a 30-min average on 10 July at 1400 LT. The background of each figure is the satellite image of the SLTEST facility where each instrument was deployed (USGS 2018)

range of turbulent sensible heat fluxes observed is large, these ranges have been previously observed in other experiments at the SLTEST site (Morrison et al. 2017).

Furthermore, periodic peaks or oscillations can be observed during the afternoon of 9 July in Figs. 5a and 7b. We hypothesize that this sawtooth pattern could be linked to coherent structures being transported over the experimental site, as similarly observed and reported by Gao et al. (2017) in the moisture flux term. Oscillations in the flux and mean-variable time series over arrays like the one presented here require further study, and may provide more insight into the spatial variability of the turbulent fluxes.

5 Total Derivative Results

Time series and ensemble averages of terms I, II, and III of Eq. 2b (i.e., terms of the total derivative) computed using the high-resolution array (10-m scales) are presented here, with

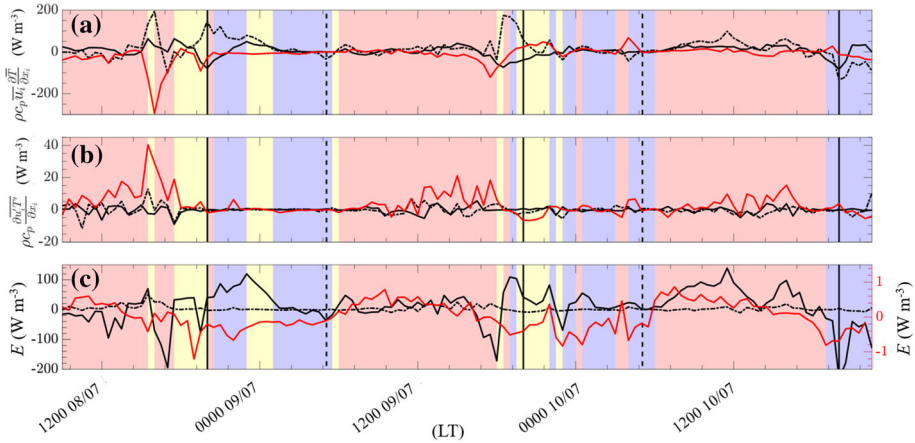


Fig. 9 Time series from 9 July to 11 July of the 2-m, 30-min tendency budget. The vertical black solid and dashed lines represent sunset and sunrise, respectively, and the background shading denotes the local stability (z/L) as in prior figures. Time series **a** of the y-component (black dashed line), x-component (solid black line), and vertical component (red line) of the advection, **b** the y-component of the flux divergence (black dashed line), x-component of the flux divergence (solid black line), and the vertical flux divergence (red line), and **c** the components of the total derivative, where advection is shown with a dashed black line, the flux divergence a solid black line, and the storage a solid red line. The right-hand axis indicates the range for the storage term (Eq. 2b, Term I) and corresponds to the red line

the terms computed following the procedure described in Sect. 2. The sign convention used is such that positive values correspond to a local cooling, and negative values correspond to local heating. Note that the plots show power per unit volume (W m^{-3}), but can also be interpreted as heating or cooling rates in K h^{-1} ; the conversion factor at the SLTEST facility is ≈ 3.6 . The results indicate that positive horizontal advection dominates the budget during afternoon convective periods, while during nocturnal periods, horizontal heating dominates. Moreover, the vertical sensible-heat-flux divergence remains slightly negative during nocturnal periods and positive and variable during afternoon convective periods.

Figure 9a shows that advection is the largest component of the total derivative. Particularly in the y-component (dashed black line), we observe that the largest spikes in advection over this time period reach 200 W m^{-3} (717 K h^{-1}) and occur during the hours leading to and just after sunset. We hypothesize that highly variable wind speeds and uneven surface cooling during the evening transition produce complex circulations which may lead to the large maxima/minima in the computed advection. Figure 9b shows that a diurnal pattern exists in the vertical sensible-heat-flux divergence (z -component), with values up to 40 W m^{-3} (143 K h^{-1}) observed during the afternoon convective period, and diminishing to a minimum near zero during the nocturnal periods. A sensitivity analysis from the treatment of the flux on the vertical flux divergence demonstrates that, over the entire experiment, the median percent difference between flux divergences computed with a constant detrend are 34% less than those computed with a linear detrend. This implies that the potential impact of this data-treatment method is to overestimate the advection term during periods where non-stationarity is present over a 30-min averaging period. The horizontal terms of the flux divergence do not appear to contribute to the overall budget, measuring $\pm 5 \text{ W m}^{-3}$ during the day, and $\pm 1 \text{ W m}^{-3}$ during stable periods. These nocturnal values of flux divergence are of similar

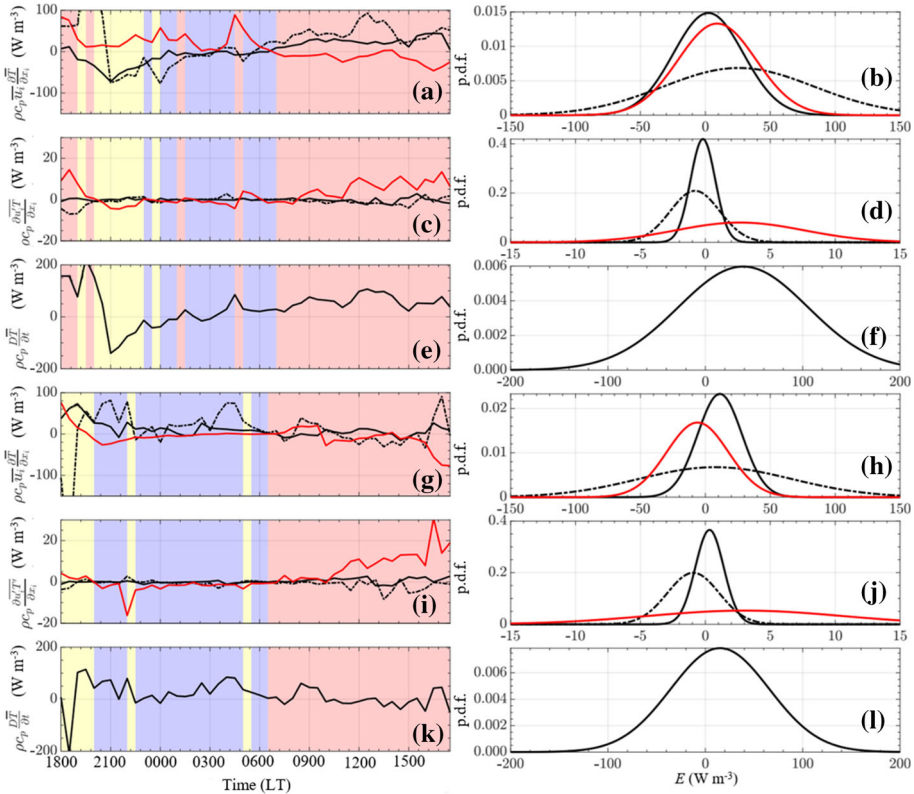


Fig. 10 A diurnal ensemble average over 3 days for each case of the terms in the total derivative for a convective (a–f) and non-convective day (g–l) as well as the corresponding p.d.f. for those terms to the right of each time series. **a** The ensemble average of the advection terms, **c** the flux-divergence terms, and **e** the total derivative for the convective days. **g** The ensemble average of the advection terms, **i** the flux-divergence terms, and **k** the total derivative for the non-convective days. In **a** through **d** and **g** through **j**, the black dashed line corresponds to the y-component, the solid black line represents the x-component, and the red line represents the z-component. The results reveal that advection is most relevant during convective days with low shear stress

order of magnitude to those computed by Nakamura and Mahrt (2006) who, however, did not compute the flux divergence for convective periods.

The composite of the total terms is presented in Fig. 9c, where the temporal evolution of the total advection, flux divergence, and storage are presented. The right-hand axis corresponds to the storage term (red line) which indicates a diurnal pattern, with persistent positive values during the day ($< 1 \text{ W m}^{-3}$) and negative values during the nocturnal period ($> -1 \text{ W m}^{-3}$). Given the range of the storage term compared with the advection and flux divergence, it is neglected in the remaining analysis.

To identify persistent patterns in the temporal signals, daily ensemble averages and corresponding probability density functions (p.d.f.s) over the free-convective (Fig. 10a, c, and e) and forced-convective days (Fig. 10g, i, and k) are presented in Fig. 10. Free-convective days are characterized by vertical motions driven by buoyant production, arising from static instability (AMS 2012). The corresponding mean wind speeds and stability for the two cases are presented in Table 2.

Table 2 Mean wind speed (\bar{U}) and stability (z/L) for the free-convective and forced-convective days isolated for the analysis

Selected day characteristics				
Period	Free-convective days		Forced-convective days	
	\bar{U} (m s ⁻¹)	z/L	\bar{U} (m s ⁻¹)	z/L
Day (1000–1600 LT)	2.7	– 8.0	4.4	– 5.0
Night (0000–0500 LT)	2.6	1.7	3.9	0.6

Figure 10a presents the advection terms for the convective days, showing persistent horizontal advective heating at night, peaking at -77 W m^{-3} (-276 K h^{-1}) in the y -component and decreasing in magnitude towards zero as the stable period concludes. Positive horizontal advective cooling during the daytime convective period measured at the high-resolution array peaks during the late morning and early afternoon periods with maximum contributions of 93 W m^{-3} (-333 K h^{-1}) in the y -component, 45 W m^{-3} (-161 K h^{-1}) in the x -component, and -46 W m^{-3} (-165 K h^{-1}) in the z -component, respectively. Figure 10g presents the advection terms for the forced-convective days, which contrasts the free-convective periods with reduced advective cooling during the daytime [average daytime advective cooling of 56 W m^{-3} (200 K h^{-1}) for free-convection cases compared with -5 W m^{-3} (-18 K h^{-1}) for the forced convection cases]. Figure 10c and i shows the ensemble average of the flux divergence terms (Eq. 2b, Term III). Averaging reveals that a slightly negative (0 W m^{-3} to -3 W m^{-3}) flux divergence persists throughout the nocturnal period, followed by a strong but variable positive vertical flux divergence in the daytime period of 10 W m^{-3} to 30 W m^{-3} . The overall result of these differences is substantiated in the p.d.f.s of the total derivative, where during convective days the total derivative mean cooling rate is 43 W m^{-3} (154 K h^{-1}) and, during the non-convective days, the cooling falls to 13 W m^{-3} (47 K h^{-1}). This result suggests that, during highly convective periods with low shear, there is a higher probability of observing large horizontal advection. This is further explained in the following section.

6 Discussion

Our results show that mean advective transport may be larger during strongly convective periods with weak mean wind speeds and persistent thermal structures than periods with strong wind speeds. We further investigate the origin of this advective heat transfer to determine whether it is locally driven (by the subjacent surface thermal heterogeneity) or forced by larger-scale (i.e., mesoscale or synoptic-scale) air displacements. Distinguishing between both types of mean advection and their contributions is important given that local advection cannot be accounted for with single-tower measurements of the SEB, and in coarse numerical weather prediction.

This discussion is built on a simple two-dimensional conceptual model of temperature advection, in which we hypothesize that advection is generated by the four different configurations illustrated in Fig. 11. For example, local advection is interpreted as a process in which flow is generated by thermally driven pressure gradients associated with localized differential surface heating (Whiteman 2000). In this case, a warmer surface would heat the air aloft, generating a change in local pressure that drives colder air from nearby to be laterally displaced, producing an overall positive advection (see Fig. 11a). This situation is representative

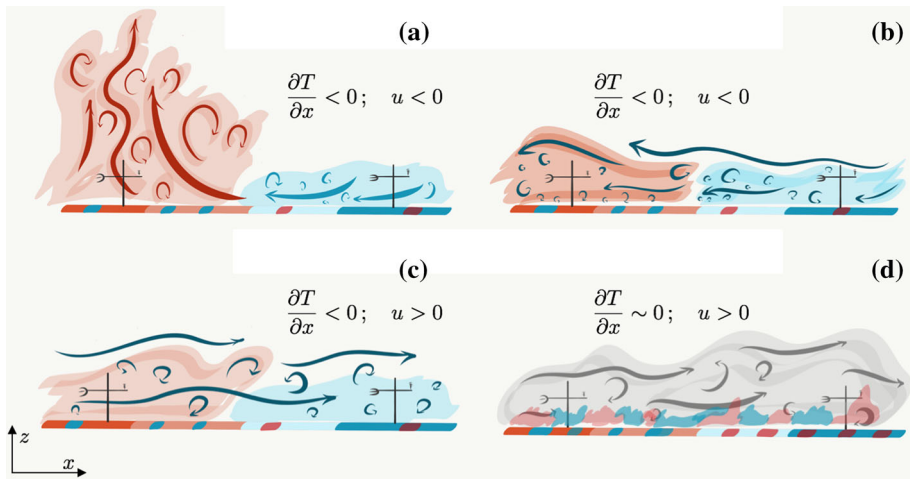


Fig. 11 Schematic of the temperature advection conceptual model at 10-m scales. Red colours indicate relatively higher temperatures, while the blue shades indicate relatively lower temperatures. The black towers indicate measurement stations and the arrows indicate the flow direction. Four possible configurations are presented: **a** an unstably stratified period corresponding to the red-coloured data points in quadrants 2 and 3 of Fig. 11. In this case, the air-temperature gradient is large, inducing strong local advection; **b** a configuration also corresponding to unstable periods (red-coloured data points), illustrated in quadrants 2 and 3 of Fig. 11), but the advection is not due to the local air-temperature differences but due to a sustained background mean flow; **c** a possible stably or neutrally stratified case (yellow and blue data points in Fig. 11) where the surface thermal gradient remains strong, but the advection is not correlated with the air-temperature heterogeneity; **d** a neutrally or stably stratified case where the surface thermal effects have been blended leading to a weak air-temperature gradient and in the presence of stronger background flow

of convective boundary-layer conditions with persistent plume-like structures. Similarly, a positive advection could also be produced with the same thermal configuration, but in the presence of an independent strong background velocity that happens to equally align with the thermal gradient. This case may be interpreted as a synoptically or mesoscale-driven positive advection (see Fig. 11b). While being able to differentiate between these two configurations remains a daunting task, we further hypothesize that local advection can be characterized by wind speeds that are lower than those associated with positive advection cases that are forced by larger scales. As a first approximation, we define a threshold between locally and larger-scale-driven advection for the IPAQS data following Margairaz et al. (2020). Using LES results, Margairaz et al. (2020) show that for wind speeds $> 4 \text{ m s}^{-1}$ the impact of the local advection (or dispersive flux) degrades rapidly depending on the surface temperature heterogeneity intensity (size and standard deviation). This threshold was identified for flow over heterogeneous temperature patches similar in scale and magnitude to that of the SLTEST facility (200–800 m surface patches and $\sigma_T = 5 \text{ K}$). This threshold requires further study and validation with other field data. Of data used in the ensemble average for Fig. 10, 38% of the advection values are positive. By assuming that local advection occurs for wind speeds $< 4 \text{ m s}^{-1}$, 69% of the positive cases could constitute local advection. Alternatively, we also envision the case of an equivalent negative advection in which the larger-scale flow is misaligned with the predominant surface-induced thermal heterogeneities (see Fig. 11c). In either of these configurations, measurements are strongly handicapped when using a single-point measurement, as represented in Fig. 11 with the corresponding schematic of the sonics occupying different thermal footprints. Lastly are the cases when the atmosphere is weakly

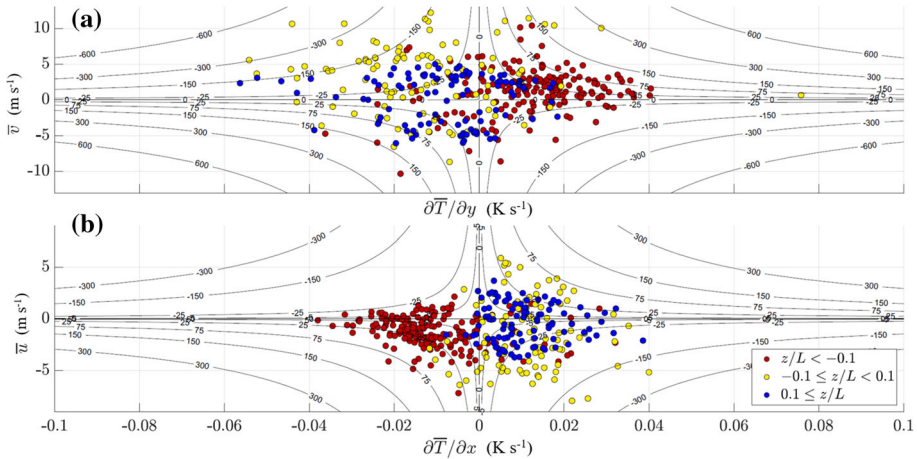


Fig. 12 Scatter plots of the **a** v - and **b** u -components of the horizontal advection terms in Eq. 2b (i.e., the horizontal velocity components versus the corresponding temperature gradient). The colour of the circles indicates the stability of the period: red unstable, yellow neutral, and blue stable. Background contours are lines of constant values of the advection term in W m^{-3}

to neutrally stratified, well mixed with small horizontal air-temperature gradients, and with background wind speeds ranging from weak to strong that lead to a smaller contribution of advection as compared with the other cases (Fig. 11d).

To further substantiate Fig. 11 with experimental data, a quadrant analysis is performed with the horizontal temperature gradients computed at the high-resolution array (10-m scale) and corresponding horizontal velocity components (Fig. 12). A key take away from the distribution of data points is the large horizontal spread, which indicates that larger air temperature gradients are observed during low-wind-speed periods. Moreover, while the data do not seem to show any a priori preferential distribution between positive and negative advection events, a clear difference appears based on stability, as illustrated through the colour of the data points (i.e., red for unstable, yellow for neutral, and blue for stable). During unstable periods, data occupying quadrant 1 for the spanwise advection account for 65% of the cases, and data in quadrant 3 for streamwise advection account for 70% of the cases. Note that either of these cases of positive advection could be interpreted as either cases (a) or (b) in Fig. 11. Furthermore, these cases could not be represented by configuration (d) in Fig. 11 given that it is representative of a neutral or stable stratification. Alternatively, the convective cases with negative advection would therefore be classified under configuration Fig. 11c. From the correlations presented here (Fig. 12), it is then possible to speculate that during unstable periods, surface thermal heterogeneities have the potential to interact with the flow and lead to persistent air temperature differences and drive at least part of the observed horizontal advection. Note that these are the cases in which horizontal advection contributed as much as 112 W m^{-3} to the temperature-tendency equation, as illustrated in Fig. 10. While we cannot fully distinguish the convective (red) data from being representative of cases (a) or (b) in Fig. 11, based on the earlier hypothesis of a weak-wind-speed threshold of 4 m s^{-1} , 83% of the unstable cases in the streamwise and 81% of the spanwise cases can be classified as local advection. Alternatively, during near-neutral and stable periods (yellow and blue dots), large variability (scatter) is observed in the correlation of the advection terms. On the other hand, during unstable periods, the vertical temperature gradient is negative, and the surface is

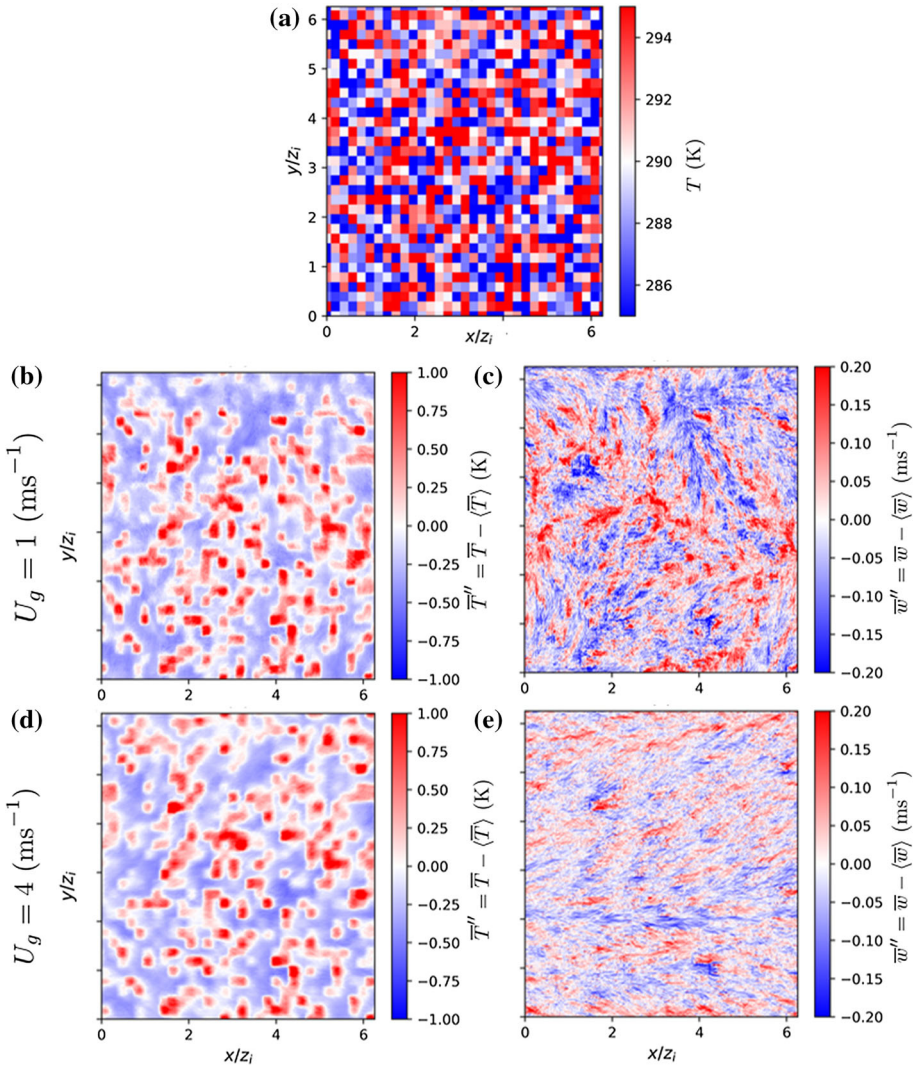


Fig. 13 LES results from Margairaz et al. (2020). **a** The bottom boundary is made up of 200-m square random surface-temperature patches. **b** and **d** are horizontal slices at 8 m of air-temperature perturbations from the horizontally averaged air-temperature field ($\overline{T}'' = \overline{T} - \langle \overline{T} \rangle$), and **c** and **e** are the spatial perturbations of vertical velocity ($\overline{w}'' = \overline{w} - \langle \overline{w} \rangle$). **b** and **c** correspond to the 1 m s^{-1} geostrophic wind-speed case and **d** and **e** correspond to the 4 m s^{-1} case. Note the decorrelation in the vertical velocity field with the temperature field as the wind speed increases from 1 m s^{-1} to 4 m s^{-1}

dynamically linked to the atmosphere through buoyant production. In stable periods, a positive temperature gradient is observed leading to situations when the surface could decouple from the flow aloft (Nieuwstadt 1984; Mahrt 1999). As a result, during stable periods, the impact of the surface is either no longer or only weakly penetrating into the air aloft, and the advection events become less correlated with the specific surface thermal forcing. Hence, this leads to more variability, as observed in Fig. 12.

To aid in the interpretation of the conceptual temperature advection model, the LES results of Margairaz et al. (2020) are presented for convective flows over idealized random-square surface-temperature patches subjected to various geostrophic wind speeds, U_g (details of the simulations can be found in Margairaz et al. 2020). Horizontal slices of the air temperature and velocity fields at the lowest grid point ($z = 8$ m) are shown in Fig. 13. The air temperature structures observed in the flow in Fig. 13b, d are induced by surface heterogeneities, which appear correlated to the vertical velocity component field during a low geostrophic wind-speed case (Fig. 13b, c, $U_g = 1$ m s⁻¹). As the wind speed increases, we observe a decoupling of the velocity field from the temperature field (Fig. 13d, e, $U_g = 4$ m s⁻¹). The decorrelation between velocity and temperature fields suggests that, during low-wind-speed periods, the observed persistent mean flow structures have a preferred organisation based on the surface-temperature forcings. Experimental evidence from the results supporting this model are shown in Fig. 12, where data points during highly convective periods occupy quadrants 1 and 3 for the spanwise and streamwise cases. While we cannot be sure if some of the observed cases are driven by large-scale advection, the combined requirement (i.e., wind speed < 4 m s⁻¹ and the components of the advection term residing in either quadrants 1 and 3 of Fig. 12) on the streamwise and spanwise advection terms increases the likelihood the cases are the result of locally driven advection.

Furthermore, the existence and intensity of locally driven advection like, the cases shown in Fig. 12, implies that single-point measurements of the turbulent flux would not be able to capture the complete heat transfer generated at the surface. As mentioned earlier, this has important ramifications for the closure of the SEB as well as for determining accurate boundary conditions in NWP models. For example, if one were to measure the total flux from the high-resolution array and were to only compute turbulent fluxes at an individual tower (or even an average from all the towers), an imbalance of the flux would occur due to the missing energy represented by the mean advection. The only way to overcome this important limitation is by either computing the local advection, or by computing the corresponding dispersive fluxes as described in Kanda et al. (2004), Inagaki et al. (2006), and Margairaz et al. (2020). The latter also provides a means of parametrizing these unaccounted heat fluxes into NWP models.

To further understand the role of advection on a strongly convective afternoon (10 July) in relation to the total heating, the contribution of the mean horizontal and vertical advective terms are plotted against the total derivative, as a function of local stability (Fig. 14), illustrating that heating of the near surface air is mostly due to horizontal advection (see Fig. 14a), while cooling is mostly due to vertical transport (see Fig. 14b). Moreover, the results show that turbulent heat transport is less efficient than mean advection transport given the quasi one-to-one relationships seen in Fig. 14c. This phenomenon was only observed on 10 July, and due to the time scales of the events, the scatter plot is presented for 1-min averages, however the same trend is observed for the 30-min-averaged data. Specifically, the percent contribution of the horizontal advection terms to the total total derivative during times when the total derivative is positive ($DT/Dt > 0$) is 76%, but only 30% when the total derivative is negative ($DT/Dt < 0$). Alternatively, the vertical advection accounts for 20% of the total derivative when $DT/Dt > 0$, and 92% when $DT/Dt < 0$. Note these values do not add to 100% since flux divergence and storage are not considered. These results agree with the explanation provided previously around Fig. 14, where under convective conditions heating is dominated by local horizontal advection. Another interesting feature from Fig. 14 is the role of local stability on the sign and intensity of the heating. For example, as the local temperature gradient decreases, buoyancy effects dominate the cooling of the local air and the vertical advection dominates (Fig. 14b). However, as the vertical temperature gradient approaches

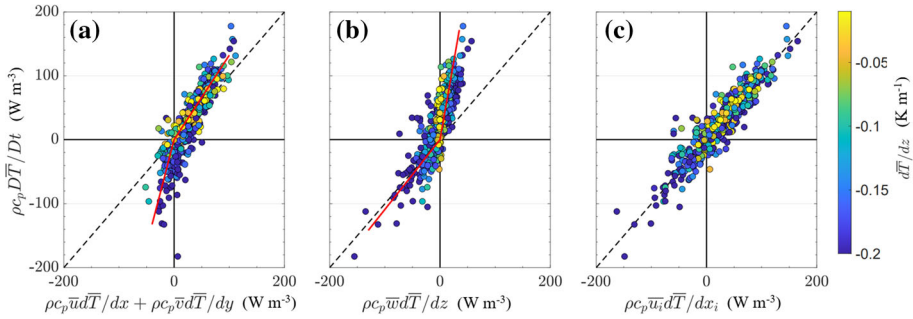


Fig. 14 Scatter plots of the total derivative as a function of advection terms for the afternoon of 10 July using 1-min averages. The black dashed line shows the one-to-one line, and the colour shows the vertical temperature gradient starting at the dry adiabatic lapse rate (-0.0098 K m^{-1}) and decreasing to -0.2 K m^{-1} . The red line in **a** and **b** shows the linear regression through the origin, excluding the centre $\pm 50 \text{ W m}^{-3}$ of the scatter to provide an estimate of the percent contribution of the horizontal advection and vertical advection during heating and cooling. **a** The horizontal advection, which encompasses 76% of the total derivative when $D\bar{T}/Dt > 0$ and 30% when $D\bar{T}/Dt < 0$. **b** The vertical advection, which is responsible for 20% of the total derivative when $D\bar{T}/Dt > 0$ and 92% when $D\bar{T}/Dt < 0$. **c** The total advection, which follows the one-to-one line closely, illustrates that advection is the primary source of energy in the total derivative. Note that, during periods with weak stratification, horizontal advection leads to heating ($D\bar{T}/Dt > 0$), while during periods of stronger stratification, vertical advection increases in magnitude

the adiabatic lapse rate, buoyancy effects are dominated by the horizontal advection (Fig. 14).

7 Conclusions

The IPAQS dataset provides a unique opportunity to study the spatial variability of near-surface sensible heat fluxes as well as the role of advection and flux divergence over an ideal flat natural surface that has uniform roughness and is heterogeneous in surface temperature. A high-density array of turbulence masts was deployed with temporal synchronization to capture spatially- and temporally-varying atmospheric flow data at sub-kilometre scales, allowing for the computation of horizontal advection and flux divergence. Maximum contributions observed in the time series of the horizontal advection peaks during the late morning and early afternoon periods (93 W m^{-3} or 328 K h^{-1} in the y -component, 45 W m^{-3} or 159 K h^{-1} in the x -component, and -46 W m^{-3} or -162 K h^{-1} in the z -component). An ensemble average of advection and flux divergence reveals a diurnal pattern with considerable peak magnitudes of 67 W m^{-3} (237 K h^{-1}) and 11 W m^{-3} (39 K h^{-1}) for convective cases, and of 57 W m^{-3} (201 K h^{-1}) and $\pm 31 \text{ W m}^{-3}$ (109 K h^{-1}) for near-neutrally stratified cases, respectively. A p.d.f. of the total derivative from the convective day cases shows mean heating rate of 43 W m^{-3} (152 K h^{-1}), while a heating rate of 13 W m^{-3} (46 K h^{-1}) was observed on non-convective days. Therefore, the results have shown that strong convective events with weak mean wind speeds can generate more intense advective heat transfer than days with stronger wind speeds and weaker thermal stratification.

To interpret this result, a conceptual model based on persistent mean-temperature perturbations in the flow arising from local surface temperature heterogeneities was presented. The model explains and defines the difference between local and large-scale-driven advection. Considering unstable cases and using a 2-m wind-speed threshold of 4 m s^{-1} , we find that

83% of the streamwise and 81% of the spanwise advection cases could be classified as being locally driven by nearby surface thermal heterogeneities. However, this threshold requires further study and may be site and stability dependent.

Our results indicate the need for the boundary-layer community to move beyond overly simplified forms of the governing equations and that local advection should be accounted for in the closure of the SEB and NWP parametrizations. Significant horizontal advection contributions to the temperature-tendency equation indicate that the assumption of horizontal homogeneity, even under the most ideal conditions, is likely to fail and lead to inaccurate accounting of the exchange of heat in the surface layer. Moreover, the vertical flux divergence has also been shown to play an important role under certain conditions, calling into question the assumption of a constant-flux layer, an assumption that is vital to scaling relationships and bulk flux calculations. Therefore, if advection and flux divergence are important in idealized environments such as the smooth playa surface studied herein, single-point flux-tower-network measurements utilized for initial conditions in climate models may suffer from these same complications.

The results presented here motivate further experimental exploration of the temperature-tendency equation. Specifically, carefully conducted experiments over heterogeneous surfaces aimed to investigate the SEB closure and to develop improved NWP boundary conditions should be performed. Further work, including more experiments with improved spatial coverage (both vertically and horizontally) deployed using surveying equipment, global positioning system synchronization, and on-site instrument calibration or collocation, are required to study the governing equations over more surface types and different flow conditions.

Acknowledgements This research was accomplished via the support of the U.S. National Science Foundation grant number PDM-1649067. Marc Calaf also acknowledges the Mechanical Engineering Department at University of Utah for start-up funds. The authors are also thankful to the U.S. Army Dugway Proving Ground for their gracious assistance and for providing the experimental test bed. The authors declare no conflict of interest.

Appendix 1: Temperature Correction

Given the anticipated errors during in situ temperature-data acquisition (panel temperature error, thermocouple error, thermocouple voltage measurement error, noise error, thermocouple polynomial error, and reference junction error), we have determined that an a posteriori temperature collocation manages these errors. Please see the Campbell Scientific CR1000 data-logger manual, pp. 343–352 for more information on these errors. Note that these are errors which arise from utilizing research-grade instruments and a temperature collocation should always be considered during future advection experiments. This methodology utilizes a second-order polynomial fit over two weeks of data between a set of *truth* measurements and a set of values needing correction. This method seeks to only correct systemic error to correct for temperature differences between stations and does not aid in finding the absolute temperatures. A second-order polynomial is selected for the correction since the errors are nonlinear across the temperatures observed during data acquisition. For our purposes, we utilized the central high-resolution-array tower as our truth tower due to its proximity to the towers utilized in the horizontal advection measurement. However, its temperature is not used in performing the temperature derivative. Thus the assumption is that over the 30 min, the towers should converge to the truth tower.

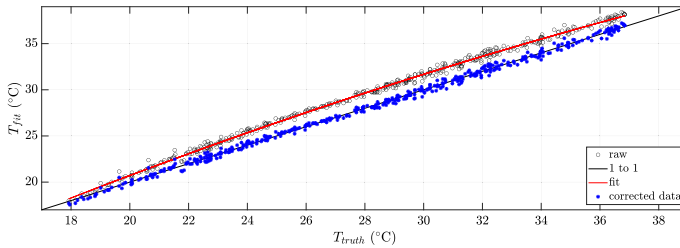


Fig. 15 An example of the 30-min averaged fine-wire temperatures from the centre high-resolution array tower (T_{truth}) against the south high-resolution array tower (T_{fit}). The black circles correspond to the raw data, where errors compile with a temperature dependency to create non-linear differences between observations. The blue stars illustrate the data with the correction applied. Each tower used in this analysis underwent the correction with the centre high-resolution array tower

An example of the temperature correction is observed in Fig. 15, which presents the 30-min-averaged *truth* temperatures against the temperature from the southern tower at the high-resolution array (10-m south from the *truth* measurements). The black circles denote the raw data, where the nonlinear trend across temperatures shows the extremes converging and the mid-valued temperatures showing the worst agreement. The black line illustrates a one-to-one fit. Meanwhile, the red line shows the parabolic fit to the data. The minimum R^2 value across all towers is 0.994, suggesting the parabolic fit works well without a dataset. Finally, the blue stars show the corrected temperature used for the computation of Eq. 2b. Note that this correction does not change the turbulent quantities and only works under cases where the absolute temperature is not needed for the final solution. Furthermore, for future applications, if the *truth* temperature was validated over a range of values observed during the experiment, then the absolute temperature could be calculated.

References

- Alfieri JG, Kustas WP, Prueger JH, Hipps LE, Evett SR, Basara JB, Neale CM, French AN, Colaizzi P, Agam N, Cosh MH, Chavez JL, Howell TA (2012) On the discrepancy between eddy covariance and lysimetry-based surface flux measurements under strongly advective conditions. *Adv Water Resour* 50:62–78. <https://doi.org/10.1016/j.advwatres.2012.07.008>
- AMS (2012) Convection: American Meteorology Society Glossary
- Aubinet M, Heinesch B, Yernaux M (2003) Horizontal and vertical CO_2 advection in a sloping forest. *Boundary-Layer Meteorol* 108:397–417
- Aubinet M, Berbigier P, Bernhofer C, Cescatti A, Feigenwinter C, Granier A, Gru T, Havrankova K, Heinesch B, Longdoz B, Marcolla B, Montagnani L, Sedlak P (2005) Comparing CO_2 storage and advection conditions at night at different carboeuroflux sites. *Boundary-Layer Meteorol* 116:63–94. <https://doi.org/10.1007/s10546-004-7091-8>
- Aubinet M, Feigenwinter C, Heinesch B, Bernhofer C, Canepa E, Lindroth A, Montagnani L, Rebmann C, Sedlak P, Van Gorsel E (2010) Direct advection measurements do not help to solve the night-time CO_2 closure problem: evidence from three different forests. *Agric For Meteorol* 150(5):655–664. <https://doi.org/10.1016/j.agrformet.2010.01.016>
- Blyth E, Gash J, Lloyd A, Pryor M, Weedon GP, Shuttleworth J (2010) Evaluating the JULES land surface model energy fluxes using FLUXNET data. *J Hydrometeorol* 11(2):509–519. <https://doi.org/10.1175/2009JHM1183.1>
- Cuxart J, Conangla L, Jiménez MA (2015) Evaluation of the surface energy budget equation with experimental data and the ECMWF model in the Ebro Valley. *J Geophys Res Atmos* 120(3):1008–1022. <https://doi.org/10.1002/2014JD022296>
- Cuxart J, Wrenger B, Martínez-Villagrada D, Reuder J, Jonassen MO, Jiménez MA, Lothon M, Lohou F, Hartogensis O, Dünnermann J, Conangla L, Garai A (2016) Estimation of the advection effects induced

- by surface heterogeneities in the surface energy budget. *Atmos Chem Phys* 16(14):9489–9504. <https://doi.org/10.5194/acp-16-9489-2016>
- Feigenwinter C, Bernhofer C, Vogt R (2004) The influence of advection on the short term CO₂-budget in and above a forest canopy. *Boundary-Layer Meteorol* 113(2):201–224. <https://doi.org/10.1023/B:BOUN.0000039372.86053.ff>
- Figuerola PI, Berliner PR (2005) Evapotranspiration under advective conditions. *Int J Biometeorol* 49(6):403–416. <https://doi.org/10.1007/s00484-004-0252-0>
- Finnigan JJ, Clement R, Malhi Y, Leuning R, Cleugh H (2003) A re-evaluation of long-term flux measurement techniques part i: averaging and coordinate rotation. *Boundary-Layer Meteorol* 107(1):1–48. <https://doi.org/10.1023/A:1021554900225>
- Foken T (2008) The energy balance closure problem: an overview. *Ecol Appl* 18(6):1351–1367. <https://doi.org/10.1890/06-0922.1>
- Foken T, Aubinet M, Finnigan JJ, Leclerc MY, Mauder M, Paw UKT (2011) Results of a panel discussion about the energy balance closure correction for trace gases. *Bull Am Meteorol Soc* 92(4):ES13–ES18. <https://doi.org/10.1175/2011BAMS3130.1>
- Gao Z, Liu H, Russell ES, Huang J, Foken T, Oncley SP (2016) Large eddies modulating flux convergence and divergence in a disturbed unstable atmospheric surface layer. *J Geophys Res Atmos* 121(4):1475–1492. <https://doi.org/10.1002/2015JD024529>
- Gao Z, Liu H, Katul GG, Foken T (2017) Non-closure of the surface energy balance explained by phase difference between vertical velocity and scalars of large atmospheric eddies. *Environ Res Lett* 12(3):034025. <https://doi.org/10.1088/1748-9326/aa625b>
- Garcia-Santos V, Cuxart J, Jimenez MA, Martinez-Villagrana D, Simo G, Picos R, Caselles V (2019) Study of temperature heterogeneities at sub-kilometric scales and influence on surface-atmosphere energy interactions. *IEEE Trans Geosci Remote Sens* 57(2):640–654. <https://doi.org/10.1109/TGRS.2018.2859182>
- Grachev AA, Fairall CW, Blomquist BW, Fernando HJ, Leo LS, Otárola-Bustos SF, Wilczak JM, McCaffrey KL (2020) On the surface energy balance closure at different temporal scales. *Agric For Meteorol*. <https://doi.org/10.1016/j.agrformet.2019.107823>
- Gunawardena N, Pardyjak E, Stoll R, Khadka A (2018) Development and evaluation of an open-source, low-cost distributed sensor network for environmental monitoring applications. *Meas Sci Technol* 29(2):024008
- Hang C, Jensen D, Hoch S, Paryjak ER (2016) Playa soil moisture and evaporation dynamics during the materhorn field program. *Boundary-Layer Meteorol* 3:521–538. <https://doi.org/10.1007/s10546-015-0058-0>
- Heusinkveld B, Jacobs A, Holtslag A, Berkowicz S (2004) Surface energy balance closure in an arid region: role of soil heat flux. *Agric For Meteorol* 122(1):21–37. <https://doi.org/10.1016/j.agrformet.2003.09.005>
- Higgins CW (2012) A-posteriori analysis of surface energy budget closure to determine missed energy pathways. *Geophys Res Lett*. <https://doi.org/10.1029/2012GL052918>
- Higgins CW, Pardyjak E, Froidevaux M, Simeonov V, Parlange MB (2013) Measured and estimated water vapor advection in the atmospheric surface layer. *J Hydrometeorol* 14(6):1966–1972. <https://doi.org/10.1175/JHM-D-12-0166.1>
- Huang YC, Brunner C, Pardyjak E, Hultmark M (2018) Simultaneous and well-resolved velocity and temperature measurements in the atmospheric surface layer. In: American geophysical union fall meeting
- Inagaki A, Letzel MO, Raasch S, Kanda M (2006) Impact of surface heterogeneity on energy imbalance: a study using LES. *J Meteorol Soc Jpn* 84(1):187–198. <https://doi.org/10.2151/jmsj.84.187>
- Jungo G, Najafi B, Puccionio M, Hoch S, Calaf M, Pardyjak E (2018) Detection and characterization of very-large-scale motions in the atmospheric surface layer through wind lidar measurements. In: American geophysical union fall meeting
- Jeglum ME (2016) Multiscale flow interactions in the complex terrain of northwestern Utah. PhD thesis, University of Utah
- Jensen DD, Nadeau DF, Hoch SW, Pardyjak ER (2016) Observations of near-surface heat-flux and temperature profiles through the early evening transition over contrasting surfaces. *Boundary-Layer Meteorol* 159:567–587
- Kanda M, Inagaki A, Letzel MO, Raasch S, Watanabe T (2004) LES study of the energy imbalance problem with eddy covariance fluxes. *Boundary-Layer Meteorol* 110(3):381–404. <https://doi.org/10.1023/B:BOUN.0000007225.45548.7a>
- Katul G, Hsieh CI, David Bowling K, Clark Shurpali N, Turnipseed A, Albertson J, Tu K, Hollinger D, Evans B, Offerle B, Anderson D, Ellsworth D, Vogel C, Oren R (1999) Spatial variability of turbulent fluxes in the roughness sublayer of an even-aged pine forest. *Boundary-Layer Meteorol* 93(1):1–28. <https://doi.org/10.1023/A:1002079602069>

- Mahrt L (1999) Stratified atmospheric boundary layers. *Boundary-Layer Meteorol* 90(3):375–396. <https://doi.org/10.1023/A:1001765727956>
- Mahrt L, Thomas CK, Grachev AA, Persson POG (2018) Near-surface vertical flux divergence in the stable boundary layer. *Boundary-Layer Meteorol* 169:373–393. <https://doi.org/10.1007/s10546-018-0379-x>
- Malek E (2003) Microclimate of a desert playa: evaluation of annual radiation, energy, and water budgets components. *Int J Climatol* 23:333–345
- Margairaz F, Pardyjak ER, Calaf M (2020) Surface thermal heterogeneities and the atmospheric boundary layer: the relevance of dispersive fluxes. *Boundary-Layer Meteorol* 175(3):369–395. <https://doi.org/10.1007/s10546-020-00509-w>
- Metzger M (2002) Scalar dispersion in high Reynolds number turbulent boundary layers. PhD thesis, University of Utah
- Meyers T, Hollinger S (2004) An assessment of storage terms in the surface energy balance of maize and soybean. *Agric For Meteorol* 125:105–115. <https://doi.org/10.1016/j.agrformet.2004.03.001>
- Moderow U, Feigenwinter C, Bernhofer C (2007) Estimating the components of the sensible heat budget of a tall forest canopy in complex terrain. *Boundary-Layer Meteorol* 123(1):99–120. <https://doi.org/10.1007/s10546-006-9136-7>
- Morrison TJ, Calaf M, Fernando HJS, Price TA, Pardyjak ER (2017) A methodology for computing spatially and temporally varying surface sensible heat flux from thermal imagery. *Q J R Meteorol Soc* 143(707):2616–2624. <https://doi.org/10.1002/qj.3112>
- Nakamura R, Mahrt L (2006) Vertically integrated sensible-heat budgets for stable nocturnal boundary layers. *Q J R Meteorol Soc* 132(615):383–403. <https://doi.org/10.1256/qj.05.50>
- Nieuwstadt FTM (1984) The turbulent structure of the stable, nocturnal boundary layer. *J Atmos Sci* 41(14):2202–2216. [https://doi.org/10.1175/1520-0469\(1984\)041<2202:TTSOTS>2.0.CO;2](https://doi.org/10.1175/1520-0469(1984)041<2202:TTSOTS>2.0.CO;2)
- Oliphant A, Grimmond C, Zutter H, Schmid H, Su HB, Scott S, Offerle B, Randolph JC, Ehman J (2004) Heat storage and energy balance fluxes for a temperate deciduous forest. *Agric For Meteorol* 126:185–201. <https://doi.org/10.1016/j.agrformet.2004.07.003>
- Oncley SP, Foken T, Vogt R, Kohsiek W, DeBruin HA, Bernhofer C, Christen A, van Gorsel E, Grantz D, Feigenwinter C, Lehner I, Liebethal C, Liu H, Mauder M, Pitacco A, Ribeiro L, Weidinger T (2007) The energy balance experiment EBEX-2000. Part I: overview and energy balance. *Boundary-Layer Meteorol* 123(1):1–28. <https://doi.org/10.1007/s10546-007-9161-1>
- Panin G, Tetzlaff G, Raabe A (1998) Inhomogeneity of the land surface and problems in the parameterization of surface fluxes in natural conditions. *Theor Appl Climatol* 60:163–178. <https://doi.org/10.1007/s007040050041>
- Prueger J, Hipps L, Cooper D (1996) Evaporation and the development of the local boundary layer over an irrigated surface in an arid region. *Agric For Meteorol* 78(3):223–237. [https://doi.org/10.1016/0168-1923\(95\)02234-1](https://doi.org/10.1016/0168-1923(95)02234-1)
- Steinfeld G, Raasch S, Markkanen T (2008) Footprints in homogeneously and heterogeneously driven boundary layers derived from a Lagrangian stochastic particle model embedded into large-eddy simulation. *Boundary-Layer Meteorol* 129(2):225–248. <https://doi.org/10.1007/s10546-008-9317-7>
- Stull RB (1988) An introduction to boundary layer meteorology. Kluwer Academic Publishers, Dordrecht
- USGS (2018) NAIP plus 7.5 of Granite Peak NW. <https://viewer.nationalmap.gov/basic/>
- Vickers D, Mahrt L (1997) Quality control and flux sampling problems for tower and aircraft data. *J Atmos Ocean Technol* 14:512–526
- Vickers D, Mahrt L (2003) The cospectral gap and turbulent flux calculations. *J Atmos Ocean Technol* 20(5):660–672. [https://doi.org/10.1175/1520-0426\(2003\)20<660:TCGATF>2.0.CO;2](https://doi.org/10.1175/1520-0426(2003)20<660:TCGATF>2.0.CO;2)
- Whiteman C (2000) Mountain meteorology: fundamentals and applications. Oxford University Press, New York
- Wilczak JM, Oncley SP, Stage SA (2001) Sonic anemometer tilt correction algorithms. *Boundary-Layer Meteorol* 99(1):127–150. <https://doi.org/10.1023/A:1018966204465>
- Williams M, Richardson AD, Reichstein M, Stoy PC, Peylin P, Verbeeck H, Carvalhais N, Jung M, Hollinger DY, Kattge J, Leuning R, Luo Y, Tomelleri E, Trudinger CM, Wang YP (2009) Improving land surface models with FLUXNET data. *Biogeosciences* 6(7):1341–1359. <https://doi.org/10.5194/bg-6-1341-2009>
- Wilson K, Goldstein A, Falge E, Aubinet M, Baldocchi D, Berbigier P, Bernhofer C, Ceulemans R, Dolman H, Field C, Grelle A, Ibrom A, Law B, Kowalski A, Meyers T, Moncrieff J, Monson R, Oechel W, Tenhunen J, Valentini R, Verma S (2002) Energy balance closure at FLUXNET sites. *Agric For Meteorol* 113(1–4):223–243. [https://doi.org/10.1016/S0168-1923\(02\)00109-0](https://doi.org/10.1016/S0168-1923(02)00109-0)
- Xu K, Pingintha-Durden N, Luo H, Durden D, Desai AR, Florian C, Metzger S (2019) The eddy-covariance storage term in air: consistent community resources improve flux measurement reliability. *Agric For Meteorol* 279(107):734. <https://doi.org/10.1016/j.agrformet.2019.107734>

Zhang Y, Liu H, Foken T, Williams QL, Liu S, Mauder M, Liebethal C (2010) Turbulence spectra and cospectra under the influence of large eddies in the Energy Balance EXperiment (EBEX). *Boundary-Layer Meteorol* 136(2):235–251. <https://doi.org/10.1007/s10546-010-9504-1>

Publisher's Note Springer Nature remains neutral with regard to jurisdictional claims in published maps and institutional affiliations.